

Purely Inertial Navigation with a Low-Cost MEMS Sensor Array

Lukas Blocher¹, Wolfram Mayer¹, Marco Arena¹,
Dušan Radović², Tobias Hiller¹
Robert Bosch GmbH¹ & Bosch Sensortec GmbH²
Reutlingen, Germany
lukas.blocher@de.bosch.com

Joachim Gerlach
Albstadt-Sigmaringen University Embedded Systems, Univ. of Tuebingen
Albstadt, Germany
gerlach@hs-albsig.de

Oliver Bringmann
Tuebingen, Germany
bringmann@informatik.uni-tuebingen.de

Abstract—This paper examines the position precision of purely inertial navigation using an array of redundant, low-cost MEMS sensors. A carefully designed IMU is used to perform navigation experiments and to analyze the benefits of a sensor array over a single sensor in practice. As our experimental results show, navigation can be improved significantly by calibrating the IMU device regarding scale factors, offsets and cross-axis sensitivity. By comparing predicted navigation error and experimental results it is shown that gyroscope angle random walk and bias instability are dominant and therefore can be used to estimate navigation performance. The latter improves roughly by a factor of $\sqrt{14}$ when using an array of 14 devices instead of a single one. A Kalman Filter with motion constraints minimizes the error when estimating positions.

Index Terms—MEMS inertial sensors, low-cost, gyroscope, accelerometer, navigation, redundancy, array, motion constraints, IMU (inertial measurement unit), Kalman Filter

I. INTRODUCTION

Purely inertial navigation is becoming more and more relevant, especially with low-cost sensors. The idea to improve navigation performance and redundancy with several sensors is becoming more common. Although there is a large number of publications dealing with the calibration or improvement of specific properties of MEMS inertial arrays [1] [2], there is almost no literature on the question of how well these arrays *actually* perform in practice [3], e.g. in simple strapdown navigation. In our paper we abstain from searching for favorable correlations [4] or optimized orientations [5] of the N individual sensors and simply rely on the \sqrt{N} improvement in noise and other normally distributed error parameters [6] by taking the sample-mean of the sensor outputs. An array of many low-cost devices may replace an expensive, high-end IMU. However, it can only do so if the final position error is at least in the vicinity of the lower bound defined by the Allan deviation characteristics – angle random walk (ARW) and bias instability (BIS) – and is not overly dominated by additional errors like vibration or offset changes appearing during the navigation period.

We intend to examine whether this lower bound may be reached when making reasonable design and calibration effort

This work was supported by the IPCEI project (BMW 16IPCEI626) by the German Federal Ministry for Economic Affairs and Energy by resolution of the German Bundestag.

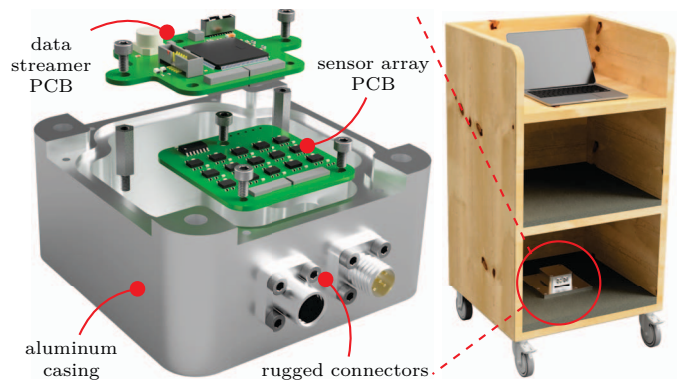


Fig. 1: Left: Exploded rendering of the redundant IMU with micro-controller PCB (printed circuit board), sensor array PCB and robust aluminum casing. Cables are not shown. Right: Hand-pushed trolley used to emulate a mobile robotics application.

and when limiting the mission profile to an elementary but still highly relevant one. A use-case in the area of mobile robotics is assumed with movement limited to the horizontal xy -plane and a room-temperature environment.

II. THEORY

A. Strapdown Mechanism & Extended Kalman Filter

Measured angular rate Ω_b and acceleration f_b is translated into attitude angles ϕ_n , θ_n , ψ_n and positions x_n , y_n , z_n from body frame b to navigation frame n by two methods here: a strapdown mechanism (SD) and an extended Kalman filter (EKF). Both are optionally supplemented by motion constraints (MC), which allow only x -direction velocity in b . In the strapdown mechanism, Fig. 2, Euler angle calculations provide the attitude rotation matrix from b to n [7]. Then gravity can be subtracted from $f_{z,n}$ and double integration yields position. For the EKF details can be found in [8]. Our state estimate vector contains positions, velocities, attitude angles and angular rate in n and acceleration and angular rate in b . The state transition equations are very similar to the strapdown. The main difference is the filtering property of the EKF provided by the model assumption that accelerations and angular rates remain constant between state updates.

B. Stochastic Sensor Errors

The potentially achievable heading and positioning precision of purely inertial navigation is limited by the stochastic errors of the sensor [9]. Allan deviation is most commonly used to differentiate and quantify various noise types. Most relevant for the time durations in this paper is the influence of gyroscope angle random walk $\sigma_{\text{ARW}} = Q/\sqrt{\tau}$ and bias instability $\sigma_{\text{BIS}} = B\sqrt{2\ln 2/\pi}$. Single integration of noisy angular rate yields zero-mean, normally distributed angle errors growing over time t with standard deviations [10]

$$\sigma_{\phi_n/\theta_n/\psi_n, \text{ARW}} = Q\sqrt{t} \quad \text{and} \quad \sigma_{\phi_n/\theta_n/\psi_n, \text{BIS}} \approx Bt. \quad (1)$$

The dominant stochastic error mechanism for typical noise values of consumer-grade MEMS accelerometers and gyroscopes is erroneous gravity compensation due to gyroscope noise impairing the attitude rotation, see Fig. 2 [10]. Compared to the double integration of accelerometer errors, the gyroscope errors are integrated three times for position output, thus growing faster over time. The normally distributed position error in the xy -plane of this mechanism is given by [10]

$$\sigma_{x_n/y_n, \text{ARW}}(t) \approx Q\sqrt{\frac{t^5}{20}} \cdot \frac{\pi}{180} 9.81 \left[\frac{\text{rad m}}{\text{deg s}^2} \right] \quad (2)$$

$$\sigma_{x_n/y_n, \text{BIS}}(t) \approx B\frac{t^3}{6} \cdot \frac{\pi}{180} 9.81 \left[\frac{\text{rad m}}{\text{deg s}^2} \right]. \quad (3)$$

Since the remaining, smaller accelerometer and gyroscope non-gravity-related noise influences are added as the square-root of the sum of squares, the total position is predicted sufficiently well by eqn. (2) and (3), see [10].

C. Systematic Sensor Errors

Systematic errors like offsets or imperfect scale-factors typically cause much larger positioning errors compared to stochastic effects in consumer-grade devices [10]. Compensation of systematic errors is essential for good positioning accuracy. The correction operations are shown in Fig. 3. Firstly, we apply a set of fixed compensation trim values to the measured input which correct offsets, scale-factors and cross-axis sensitivities [11]. The trim was generated by calibration on a rate table. Secondly, we use a 10 s duration of rest before each experiment to zero the gyroscope offsets again, calculate the initial angles from gravity and normalize the accelerometer vector to 1 g. The correction procedure is the same and is independent of the navigation algorithm involved.

D. Motion Constraints

In many mobile robots movement occurs only in the “forward” direction of the vehicle whereas sideways motion is physically impossible. Two wheels of our trolley are fixed, largely eliminating drifting motion during curves. Motion constraints are thus formulated in the navigation algorithms by transforming the calculated velocities v_n to body frame, allowing only the passing of $v_{x,b} \neq 0$ and transforming back to the navigation frame before integrating to position. The respective current rotation matrices are taken from the attitude rotation block. Figure 3 visualizes this idea. EKF-MC works analogously.

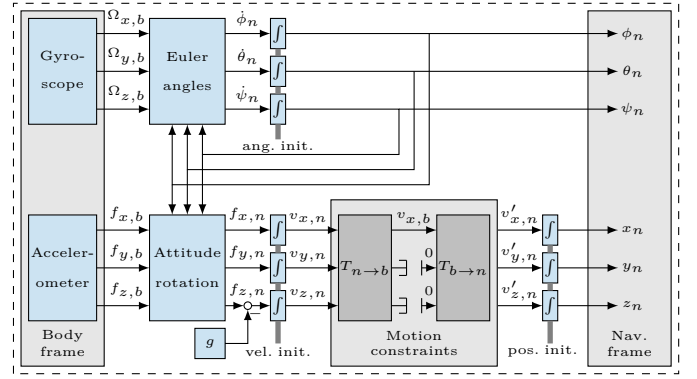


Fig. 2: Schematic of strapdown mechanism (SD) with rotation of measurements from the body to the navigation frame [7] [8] [10]. The motion constraints (SD-MC) prevent sideways and up/down velocities of the vehicle in the body frame.

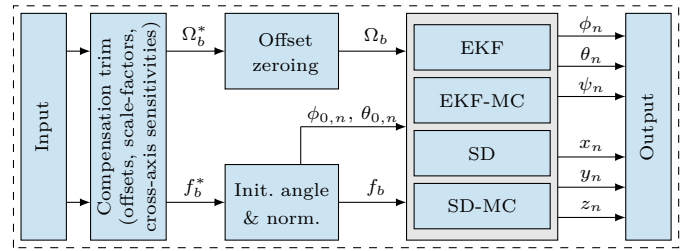


Fig. 3: Schematic of Matlab/Simulink data-processing [8]. A fixed compensation trim derived from an earlier calibration is applied to the measured input. Before each experiment, gyroscope offset is zeroed, initial orientation angles $\phi_{0,n}$ and $\theta_{0,n}$ are calculated and the accelerometer triad is normed to 1 g.

III. EXPERIMENTS

A. Setup

Our sensor array PCB contains 14 six degrees of freedom BMI090L devices as shown in Fig. 1. The consumer-grade sensors are designed for high vibration robustness and offset stability, facilitated by the gyroscopes' operation in closed-loop, quadrature-compensated fashion. The PCB has small form-factor of 47×47 mm with a three-point mounting to reduce stress effects. A micro-controller sends and receives SPI signals and streams the measured data to a laptop via USB cable. The navigation solution is calculated in Matlab/Simulink in post-processing. Sensor array and micro-controller PCB are separated in order to reduce thermal stress influences. Both are housed within a milled, airtight aluminum casing to shield the sensors from humidity and temperature variations.

Experiments are performed with a hand-pushed trolley on a shop-floor, see Fig. 1. The mission profile is rectangular with a perimeter of 38 m over the course of 30 s. Start and end positions are identical, allowing simple evaluation of the final navigation solution error without the need of an external reference system. Some hours before all experimental runs we performed a 6-point calibration using a stimulus of ± 1 g and ± 200 dps on each axis on a highly precise rate table, see Fig. 5. The procedure is outlined in detail in [11]. Other calibration mechanisms, even the ones without a rate table, would also be possible to generate the compensation trim, e.g. [12].

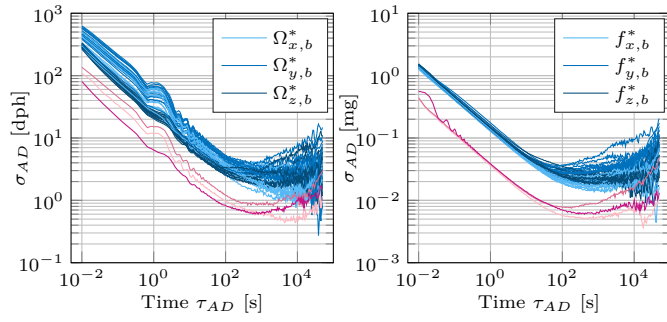


Fig. 4: Allan deviation of 14 devices (blue) measured for 48 h of gyroscopes (left) and accelerometers (right). The sample mean of all sensors' output for each axis is shown in shades of red for the x , y and z -axis.

B. Position Error Prediction

The Allan deviation in Fig. 4 allows extraction of the ARW and BIS levels for the sample mean signal (red shades): $Q_x = 3.0$ mdps/rHz, $Q_y = 4.0$ mdps/rHz, $B_x \sqrt{2 \ln 2 / \pi} = 0.5$ dph and $B_y \sqrt{2 \ln 2 / \pi} = 0.8$ dph. The total position error is defined as the euclidean norm $|\vec{\sigma}_{err}|$ of the error vector

$$\vec{\sigma}_{err} = \begin{bmatrix} \sigma_{x_n} \\ \sigma_{y_n} \end{bmatrix} = \begin{bmatrix} \sqrt{\sigma_{y_n,ARW}^2 + \sigma_{y_n,BIS}^2} \\ \sqrt{\sigma_{x_n,ARW}^2 + \sigma_{x_n,BIS}^2} \end{bmatrix}. \quad (4)$$

The predicted 1-sigma position error caused by BIS and ARW is calculated by using eqn. (2) and (3). For a navigation time of $t = 30$ s this results in an analytically predicted 1-sigma position error of $|\vec{\sigma}_{err}| = 0.99$ m, shown in Table I.

C. Navigation Experiments

Each navigation experiment was executed by hand-pushing the trolley along the rectangular path shown in Fig. 8. Overall position error is measured between start (0,0) and endpoint of the experiment: $\vec{d} = [x_{n,end} \ y_{n,end}]^T$. In advance of each experiment a 10 s duration of rest is used to collect data for gyro offset zeroing, accel normalization to 1 g and initial angle calculation. Using this procedure a total of five data-sets labeled A to E with a purely inertial navigation duration of 30 s each were recorded. The position paths using the individual sensors compared to the entire sensor array are shown in Fig. 5 for experiment A. The red path was generated by taking the sensors' sample mean, SD algorithm and applying motion constraints. Fig. 6 is a zoomed view of the bottom right corner of Fig. 5. It clearly shows how position estimation can benefit from a detailed physical model of the involved vehicle by applying specific motion constraints and therefore suppressing sideways drift.

Table I: Position error prediction caused by ARW and BIS noise using eqn. (2) and (3), extracted from Fig. 4. The absolute position error results from calculating the euclidean norm of x - and y -axis error components.

error	ARW	BIS	combined	units
σ_{x_n}	0.75	0.26	0.80	[m]
σ_{y_n}	0.57	0.16	0.59	[m]
$ \vec{\sigma}_{err} $	0.94	0.30	0.99	[m]

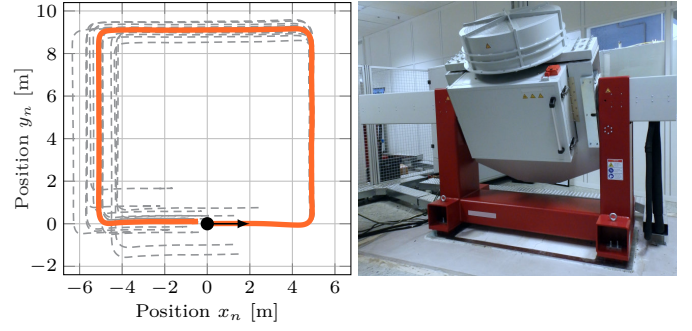


Fig. 5: Left: Bird's eye view of calculated positions with constrained motion (SD-MC) for the individual sensors (gray, dashed) compared to the sensors' sample mean (orange). The black dot indicates the start and end point, the arrow illustrates movement direction. Right: A highly-accurate rate table.

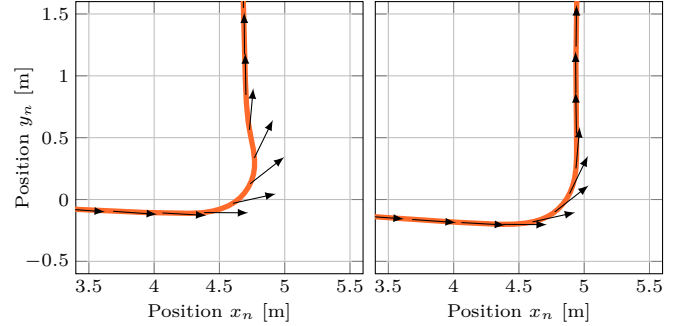


Fig. 6: Detailed view of the first left curve from Fig. 5 showing the result of the sensors' sample mean (orange) and heading direction (black) based on experiment A without (SD, left) and with motion constraints (SD-MC, right).

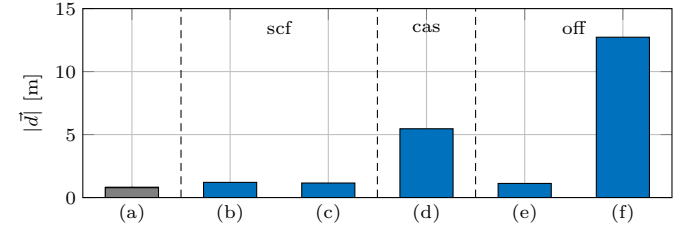


Fig. 7: Position error of experiment D with SD algorithm and all compensations enabled (a, gray) compared to results with single components disabled: gyroscope (b) and accelerometer (c) scale-factors, cross-axis sensitivity of both triads (d), and offsets of gyroscope (e) and accelerometers (f).

D. Contribution of Compensation Methods

The impact of the individual compensation methods is summarized in Fig. 7. Bar (b) to (f) compare the position error occurring when single compensations are disabled. The analysis was based on experiment D as shown in Fig. 9. It is clearly visible that the major error components introduced are cross-axis sensitivity and accelerometer offsets. To deal with the non-orthogonalities and accel-to-gyro triad alignment, which are aggregated in cross-axis sensitivity, the whole IMU device needs to be calibrated. This was done using the 6-point calibration, as proposed. The compensation for accelerometer offsets takes place before each measurement by keeping the set-up steady and normalizing the triad to 1 g.

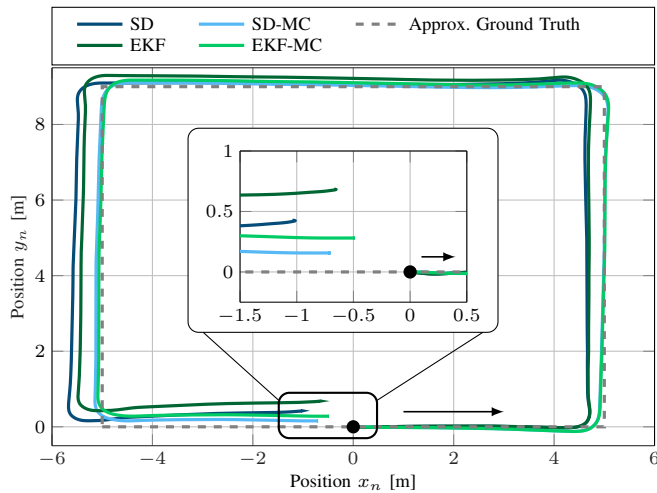


Fig. 8: Direct comparison of position accuracy after 30 s of the four algorithms in experiment A. Inset: Zoomed view onto the start (black dot) and end point of the experiment.

E. Discussion

Fig. 8 visualizes all four algorithms applied to experiment A. Overall position error resulting from the different algorithm approaches is highlighted in the zoomed inset. Under these conditions the EKF-MC performs best. This finding is supported by comparing all five recorded experiments as shown in Fig. 9. The EKF outperforms the SD consistently by approx. 10 %. The additional application of motion constraints leads to an improvement of roughly 25 % in both methods. A usage of constraints results in the predicted position being noticeably closer to the ground truth by suppressing erroneous sideways drift. This approach does not only improve overall error, but also congruence of ground truth and prediction during navigation. Of course, the design of specific motion constraints matching the vehicle physics is required. If the simple strapdown algorithm is used, the expected 1-sigma position error may be approximated exclusively based on gyroscope angle random walk and bias instability. The results show that our redundant inertial sensor array can indeed perform close to this theoretical target as shown by the hatched area in Fig. 9.

Nonetheless, there is still some limited deviation from the prediction level, which leads to the conclusion that further error sources are present. These could include temperature or vibration effects and further investigation is needed here. The impact of the particular navigation trajectory also needs to be considered. Choosing a different scenario may introduce other angular velocities and include less straight movement. This could cause the EKF to perform worse than in the scenario shown, since the filter benefits from near-zero changes in direction due to its low-pass filtering attributes. We have shown that the \sqrt{N} improvement of noise parameters holds true for 14 devices. How far the \sqrt{N} rule will keep its validity as more and more sensors are added to the array still has to be investigated.

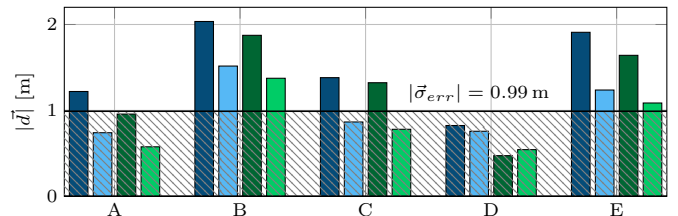


Fig. 9: Comparison of the total xy -position error $|\vec{d}|$ using the four algorithms SD (dark blue), SD-MC (light blue), EKF (dark green) and EKF-MC (light green) in five similar experiments A to E with a duration of 30 s each. The hatched box represents the 1-sigma error prediction based on the $\sqrt{14}$ -improved gyroscope angle random walk and bias instability levels.

IV. CONCLUSION

We demonstrated that an array of 14 low-cost MEMS inertial sensors can indeed reach position accuracies that are not too far off from the 1-sigma error prediction calculated from angle random walk and bias instability magnitudes. The improvement of noise matched the theoretical \sqrt{N} prediction. Thoughtful hardware design and systematic error calibration were essential. Especially cross-axis sensitivity and accelerometer offset compensation were critical for good navigation results. Position estimation and therefore feasible purely inertial navigation time can be enhanced by careful algorithm selection and may be supplemented with additional knowledge regarding vehicle physics by applying motion constraints.

REFERENCES

- [1] J.-O. Nilsson and I. Skog, "Inertial sensor arrays – A literature review," in *2016 ENC*. IEEE, 2016, pp. 1–10.
- [2] H. Kamata, M. Kimishima, T. Sawada, Y. Suga, H. Takeda, K. Yamashita, and S. Mitani, "MEMS gyro array employing array signal processing for interference and outlier suppression," in *2020 IEEE INERTIAL*. IEEE, 2020, pp. 1–4.
- [3] I. Skog, J.-O. Nilsson, and P. Händel, "Pedestrian tracking using an IMU array," in *2014 IEEE International Conference on Electronics, Computing and Communication Technologies (CONECCT)*. IEEE, 2014, pp. 1–4.
- [4] J. Wang and E. Olson, "High-performance inertial measurements using a redundant array of inexpensive gyroscopes (RAIG)," in *2015 IEEE Int. Conference on Multisensor Fusion and Integration for Intelligent Systems (MFI)*. IEEE, 2015, pp. 71–76.
- [5] H. Martin, P. Groves, M. Newman, and R. Faragher, "A new approach to better low-cost MEMS IMU performance using sensor arrays," in *26th ION GNSS 2013*. Institute of Navigation (ION), 2013, pp. 2125–2142.
- [6] D. S., "Combining multiple gyroscope outputs for increased accuracy," *NASA Tech Briefs*, vol. 28, no. 4, pp. 36–37, June 2003.
- [7] D. Titterton and J. L. Weston, *Strapdown inertial navigation technology*. IET, 2004, vol. 17.
- [8] W. Mayer, "Erhöhung der Genauigkeit rein inertialer Indoor Navigation mittels redundanter MEMS Sensorik und innovativer Algorithmen," Contact: pub.wolfram.mayer@gmail.com, Bachelor's thesis, Duale Hochschule Baden-Wuerttemberg, 2020.
- [9] T. Hiller, Z. Pentek, J.-T. Liewald, A. Buhmann, and H. Roth, "Origins and mechanisms of bias instability noise in a three-axis mode-matched MEMS gyroscope," *IEEE Journal of Microelectromechanical Systems*, vol. 28, no. 4, pp. 586–596, Aug. 2019.
- [10] T. Hiller, "Highly precise MEMS gyroscopes for fully automated driving," Ph.D. dissertation, University of Siegen, 2021.
- [11] T. Hiller, L. Blocher, M. Vujadinovic, Z. Pentek, A. Buhmann, and H. Roth, "Analysis and compensation of cross-axis sensitivity in low-cost MEMS inertial sensors," in *IEEE Int. Symposium on Inertial Sensors and Systems*. IEEE, March 2021, in press.
- [12] J. Rohac, M. Sipos, and J. Simanek, "Calibration of low-cost triaxial inertial sensors," *IEEE Instrumentation & Measurement Magazine*, vol. 18, no. 6, pp. 32–38, 2015.